

Variational Image Feature Extraction for the EHT

PAUL TIEDE,^{1,2,3} AVERY E. BRODERICK,^{1,2,3} AND DANIEL C. M. PALUMBO^{4,5}

¹ *Perimeter Institute for Theoretical Physics, 31 Caroline Street North, Waterloo, ON, N2L 2Y5, Canada*

² *Department of Physics and Astronomy, University of Waterloo, 200 University Avenue West, Waterloo, ON, N2L 3G1, Canada*

³ *Waterloo Centre for Astrophysics, University of Waterloo, Waterloo, ON N2L 3G1 Canada*

⁴ *Black Hole Initiative at Harvard University, 20 Garden Street, Cambridge, MA 02138, USA*

⁵ *Center for Astrophysics — Harvard & Smithsonian, 60 Garden Street, Cambridge, MA 02138, USA*

ABSTRACT

Imaging algorithms form powerful analysis tools for VLBI data analysis. However, these tools cannot measure certain image features (e.g., ring diameter) by their non-parametric nature. This is unfortunate since these image features are often related to astrophysically relevant quantities such as black hole mass. This paper details a new general image feature extraction technique that applies to a wide variety of VLBI image reconstructions called *variational image domain analysis*. Unlike previous tools, variational image domain analysis can be applied to any image reconstruction regardless of its structure. To demonstrate its flexibility, we analyze thousands of reconstructions from previous EHT synthetic datasets and recover image features such as diameter, orientation, and asymmetry. By measuring these features, VIDA can help extract astrophysically relevant quantities such as the mass and orientation of M 87.

Keywords: black hole physics — Galaxy: M87 — methods: data analysis — methods: numerical — submillimeter: imaging

1. INTRODUCTION

Generating quantitative measurements about intrinsic radio images from very long baseline interferometry (VLBI) is a computationally and theoretically difficult task. This is especially true for the Event Horizon Telescope (EHT) due to its sparse coverage (Event Horizon Telescope Collaboration et al. 2019a) in the visibility domain. To deal with this problem, the EHT used two separate analyses in its first results on M 87 (Event Horizon Telescope Collaboration et al. 2019b). The first was a traditional Bayesian parametric modeling approach (Event Horizon Telescope Collaboration et al. 2019c, hereafter Paper VI). In Paper IV, imaging methods demonstrated that M 87 is ring-like. Here, simple geometric models were fit to the visibility data, and direct inferences about the image properties, e.g., diameter, were possible. The other approach is non-parametric and usually referred to as imaging (Event Horizon Telescope Collaboration et al. 2019d, hereafter Paper IV). Imaging includes deconvolution algorithms like CLEAN

(Högbom 1974; Schwarz 1978; Clark 1980; Schwab 1984) and forward modeling approaches such as “maximum entropy” (Frieden 1972; Gull & Daniell 1978; Narayan & Nityananda 1986), regularized maximum likelihood (RML) (Chael et al. 2016, 2018; Akiyama et al. 2017a,b), and Bayesian imaging (Broderick et al. 2020). The output of imaging is a set of image reconstructions that reproduce the observed visibility data. Unlike parametric modeling, imaging methods do not give direct quantitative measurements of image features such as ring diameter, width, orientation, etc. Instead, an additional processing step is needed to extract image features.

In Paper IV and Paper VI, quantitative image features were extracted by the algorithm “ring extractor” ReX (Chael 2019). However, ReX is only applicable to images that have a dominant ring-like feature. In general, images from the EHT can have a complex structure and are dependent on the intrinsic source. For instance, the active galactic nuclei 3c 279 displays a jet morphology which can be described by a set of Gaussians. In this case, the features of interest are the motions of the Gaussian complexes (Kim et al. 2020). Therefore, a more general technique that applies to a variety of image structures is needed.

One possible approach to feature extraction would be to “filter” out the relevant image features using a transformation. For example, the Hough transform (Hough 1964; Duda & Hart 1972), is used to extract rings and other shapes from images using template matching. A related method approximates the image with parametric objects or *filters* that describe the features of interest. This idea is more akin to the parametric/forward modeling approach of visibility data Paper VI and is the approach taken in this paper. We call this approach *variational image domain analysis* or VIDA, due to its similarity to variational inference, as will be explained below. The benefit of VIDA is that it can easily be extended to various image morphologies by using different parameterized filters. This paper uses geometric objects as filters; however, any parametric flux distribution would work.

The layout of the paper is as follows: In Section 2, we present the details of VIDA. We present the different types of filters we use in this paper, and the objective function used to find the best approximation to the true image. Section 3 applies VIDA to a variety of ring-like image reconstructions from the test set of Paper IV and compares the results to ReX. Next, in Section 4, we demonstrate VIDA’s flexibility by applying it to non-ring images from the test set of Paper IV. Finally, the conclusions are detailed in Section 5.

2. VARIATIONAL IMAGE DOMAIN ANALYSIS

The critical insight behind VIDA is that images (sans polarization) and probability densities (modulo overall flux) are in one to one correspondence. Namely, images are point-wise positive and integrable. Therefore, we use probability divergences as the objective function between the image reconstruction and the filter. VIDA is thus similar to variational inference (VI), where typically the Kullback Leiber (KL) divergence (Kullback & Leibler 1951) is used. We will review probability divergences and the examples used in this paper in Section 2.2. VIDA thus consists of three ingredients:

1. **Image** $I(\alpha, \beta)$ whose features we want to extract
2. **Filter** (or approximate image) that parameterizes the features of interest, e.g. ring radius
3. A **divergence**, i.e. the objective function we minimize

Each of these ingredients has been implemented in the Julia package VIDA.jl¹. In Section 2.1 and 2.2 we will

review the filters and divergences currently implemented in VIDA respectively.

2.1. Image Filters in VIDA.jl

The choice of filter used will depend on the structure of the image. For example, the images of M 87 from Paper IV are ring-like, while the reconstructions of 3c 279 from Kim et al. (2020) can be described by several Gaussian brightness distributions. In this section, we present the various filters that are implemented in VIDA.jl. Note that other filters can be added with minimal effort from the user and can be constructed by simply adding the current filters to form composite filters².

2.1.1. Gaussian Filter

To model a source of compact flux we include an asymmetric Gaussian filter. The parameters of the Gaussian filter are:

1. The size, $\sigma = \sqrt{\sigma_a \sigma_b}$, where $\sigma_{a,b}^2$ are the variances in the principal directions of the Gaussian.
2. The asymmetry, $\tau = 1 - \sigma_b/\sigma_a$, measures the asymmetry of the Gaussian and we assume $\sigma_a > \sigma_b$.
3. ξ , rotation angle (relative to the Gaussian center) of the principal axes measured east of north.
4. x_0, y_0 , the center of the Gaussian.

2.1.2. Disk Filter

In Section 3 we will test VIDA.jl on a number of synthetic data tests. One of the tests images is a disk. To approximate disks we use the filter function:

$$f_{\text{Disk}}(r; r_0, \alpha, x_0, y_0) = N \begin{cases} 1 & r < r_0 \\ \exp(-(r - r_0)^2/2\alpha^2) & r > r_0, \end{cases} \quad (1)$$

where r_0 is the radius of the flat disk, α controls the smoothness of fall off and N ensures the filter is normalized. The radial distance, r , is relative to the center x_0, y_0 and N is the normalization. When $r_0 = 0$ this filter reduces to a symmetric Gaussian with standard deviation α .

¹ <https://github.com/ptiede/VIDA.jl>

² See the documentation at <https://ptiede.github.io/VIDA.jl/dev/>.

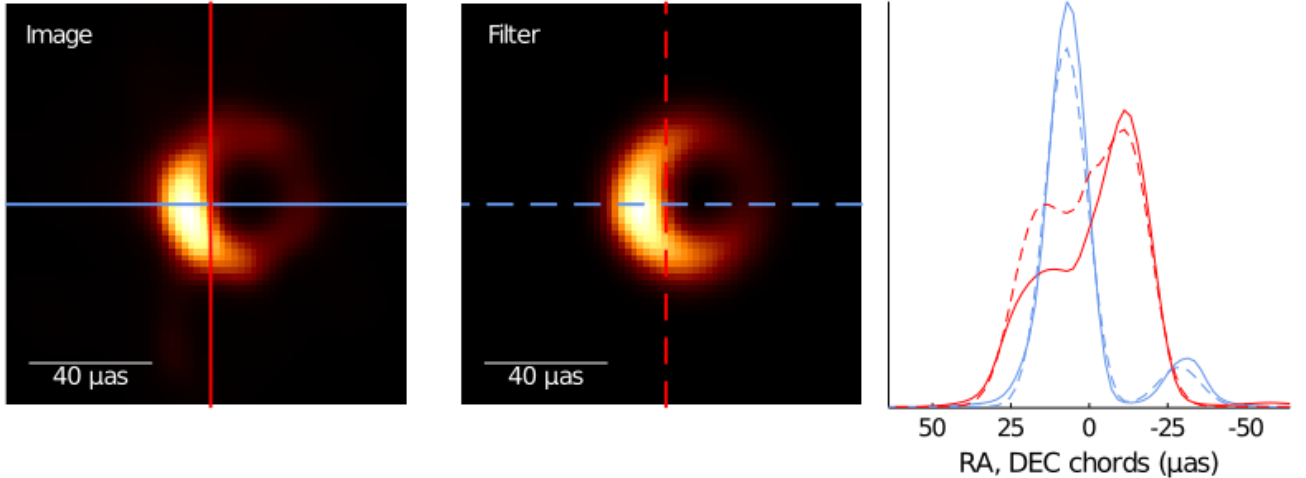


Figure 1. An example of VIDA run. *Left:* image reconstruction of a GRMHD simulation from Paper V; Paper IV. *Middle:* VIDA reconstruction using the `GeneralGaussianFilter` and Bh divergence. *Right:* vertical (red) and horizontal (blue) chords through the center of light of the truth image. The dashed lines are for the VIDA optimal filter, and solid for the reconstruction. This plot can be made in the `VIDA.jl` package using the `triptic` function and is used to assess the quality of the filter approximation.

2.1.3. Ring Filters

One of the principal quantities of interest in images of M 87 is the ring diameter, d_0 since it is related to the mass of the central black hole. Additionally, the ring is expected to have some thickness, w , due to the emitting material around the black hole. The simplest filter would be a circular Gaussian ring with some thickness. Doppler boosting, however, can cause the emission to appear asymmetric. A slash can be added to the ring filter to include the brightness asymmetry. Additionally, the ring itself does not have to be circular. Ring asymmetry could occur from, for example, the emitting material not being azimuthally symmetric around the black hole. As well, due to the sparse coverage of the EHT array and the ad-hoc nature of imaging algorithms, the reconstructions may be more elliptical than the truth. Consolidating each of these features into a filter parameter, we get the following:

- d_0 : the geometric mean of the semi-major, a , and semi-minor, b , axis $d_0 = 2\sqrt{ab}$ which is related to the area of the ellipse, $\pi(d_0/2)^2$.
- τ : the asymmetry of the ellipse, $\tau = 1 - b/a$
- ξ_τ : the position angle of the semi-major axis measured north of east.
- w : the width of the Gaussian ring, defined to be the full width half max (FWHM) of the Gaussian, i.e. $w = 2\sqrt{2\log 2}\sigma$, where σ is the standard deviation.

- s : the strength of the slash described in equation (4).
- ξ_s : the position angle of the slash measured east of north.
- (x_0, y_0) : the center of the ring.

The functional form of the filter is given by:

$$h_\theta(x, y) = S(x, y; s, \xi) \exp\left[-\frac{(d_\theta(x, y))^2}{2\sigma^2}\right], \quad (2)$$

where $S(x, y; s, \xi)$ is the slash function and $d_\theta(x, y)$ is the minimum distance between the ellipse with parameters $\theta = d_0, \tau, x_0, y_0$ and the point x, y . If $\tau = 0$, $d_{\tau=0}(x, y) = |\|\mathbf{x} - \mathbf{x}_0\| - d_0/2|$. However, for an ellipse there is no analytical equation and instead one has to numerically minimize the function,

$$L(x, y, e_x, e_y) = \|(x - e_x, y - e_y)\|, \quad (3)$$

subject to the constraint that e_x, e_y are points on the ellipse with parameters d_0, τ, ξ_τ .

For the slash function S , we use a first order cosine expansion in azimuthal angle ϕ around the center x_0, y_0 :

$$S(x, y; s, \xi_s) = N_0 [1 + s \cos(\phi - \xi_s)], \quad (4)$$

where N_0 is a normalization factor to ensure the filter is unit normalized. To prevent image flux from becoming negative, we restrict $s \in [0, 1]$. In the `VIDA.jl` package, this filter is called `GeneralGaussianRing` (GGR).

Additionally, `VIDA.jl` has a number of other ring-like filters currently implemented:

- **GaussianRing**: Symmetric Gaussian ring with constant azimuthal intensity (i.e. GGR with $\tau, s = 0$)
- **SlashedGaussianRing**: Symmetric Gaussian ring with azimuthal slash described by Equation 4 (i.e. GGR with $\tau = 0$)
- **EllipticalGaussianRing**: Elliptical Gaussian ring with constant azimuthal flux (i.e. GGR with $s = 0$)
- **TIDAGaussianRing**: GGR filter where the slash and asymmetry position angle are either aligned or anti-aligned.

We also include a more general version of the GGR called the **CosineRing** $\{N, M\}$. This filter is similar to the GGR filter but where the width, σ , and slash function (4) are replaced by a higher order cosine expansion in azimuthal angle ϕ :

$$S_M(\phi; \mathbf{s}, \boldsymbol{\xi}^{(s)}) = 1 - \sum_{m=1}^M s_m \cos \left[m(\phi - \xi_m^{(s)}) \right], \quad (5)$$

$$\sigma_N(\phi; \boldsymbol{\sigma}, \boldsymbol{\xi}^\sigma) = \sigma_0 + \sum_{n=1}^N \sigma_n \cos \left[n(\phi - \xi_n^{(\sigma)}) \right]. \quad (6)$$

We can reproduce the **GeneralGaussianRing** filter by setting $M = 1$ and $N = 0$ in (5) and (6) respectively. This filter can be used if image has a ring-like feature that has a bumpy azimuthal profile.

2.1.4. Constant Filter

We found that many image reconstructions had a diffuse amount of flux throughout the image due to poor dynamic range from sparse coverage and regularization effects. To model the background, we added a constant flux filter. This filter is typically required to be included in any analysis to ensure reliable feature extraction.

2.2. Probability Divergences

As mentioned above **VIDA.jl** uses an analogy between images and 2-D probability distributions. Divergences form a general way to measure the similarity between two distributions. A divergence can be thought of as a functional $J_q[p] = \mathcal{D}(p||q)$, comparing a the distribution p (filter) to a reference q (image), and is required to be non-negative, $\mathcal{D}(p||q) \geq 0$, and non-degenerate, $\mathcal{D}(p||q) = 0$ if and only if $p = q$. Note that this definition is more general than a metric. Namely, a divergence does not have to be symmetric, i.e. $\mathcal{D}(p||q) \neq \mathcal{D}(q||p)$ or satisfy the triangle equality.

One of the most well-known divergences is the Kullback-Leiber (KL) divergence or relative entropy,

$$KL(p||q) = \int p(x) \log \left(\frac{p(x)}{q(x)} \right) d^2x. \quad (7)$$

Variational inference usually uses a quantity related to the KL divergence, although other divergences are possible (e.g. [Ranganath et al. 2016](#)).

In addition to the KL divergence another example is the Bhattacharyya divergence (Bh) ([Bhattacharyya 1943](#)),

$$Bh(p||q) = -\log \int \sqrt{p(x)q(x)} d^2x. \quad (8)$$

An important feature of both the KL and Bh divergence is that they are parameterization independent. Namely, if we transform from $x \rightarrow f(x)$ where f is a smooth invertible map, we find that Bh and KL are invariant.

VIDA.jl implements both of the KL and Bh divergence; however, others will be added in the future. During our tests, we found that the Bh and KL divergence gave very similar results but that the Bh divergence was much easier to optimize. Therefore, in this paper, we use the Bh divergence exclusively.

2.3. Minimizing the Divergence

A problem when using probability divergences is that they tend to form non-convex, non-linear optimization problem. These features imply that typical gradient optimization algorithms will get trapped in local minima. Therefore, to extract the optimal filter, we turned to heuristic global optimizers, such as Genetic/Evolutionary strategies (see [Das & Suganthan 2011](#), for a review) and simulated annealing ([Goffe 01 Oct. 1996](#)). The Julia language has a number of different optimization packages such as **Optim.jl** ([Mogensen & Riseth 2018](#)), **BlackBoxOptim.jl**³. **VIDA** currently has interfaces to both packages and will add others in the future. In our experiments, we found that **BlackBoxOptim.jl** and its default optimizer tended to be the most robust to local minima. **BlackBoxOptim.jl** uses a differential evolution strategy to optimize the function.

3. VALIDATING VIDA

In this section we will first review the set of images that was used in [Paper IV](#) to test **ReX**. Next we will run **VIDA** on these test cases and compare the results to **ReX**.

3.1. Image Reconstruction Topset

³ <https://github.com/robertfeldt>

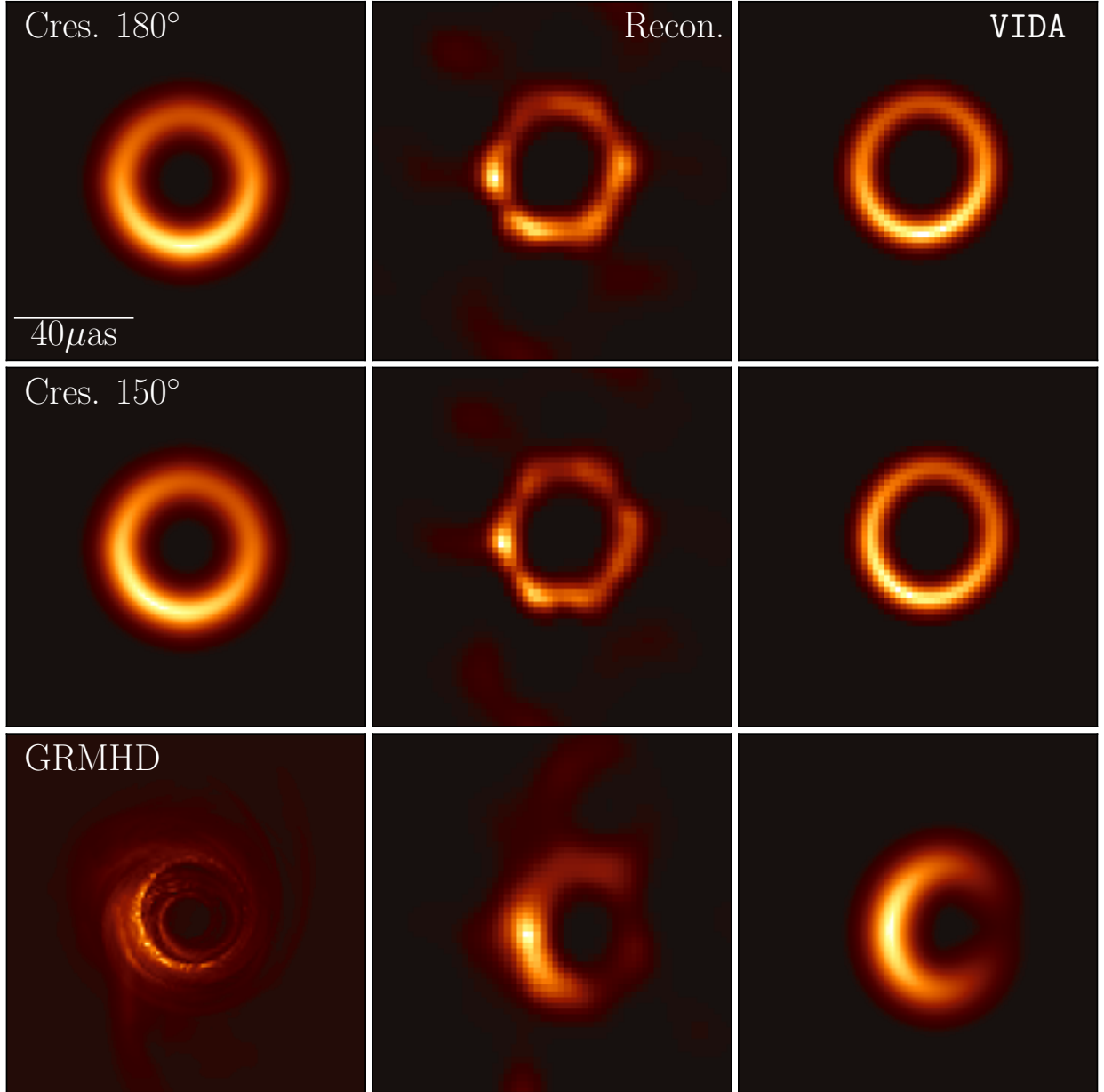


Figure 2. Images used for the imaging validation from [Event Horizon Telescope Collaboration et al. \(2019d\)](#). We considered 3 models: *top row* crescent with position angle $\xi = 180^\circ$ north of east, *middle row* crescent with position angle $\xi = 150^\circ$ and *bottom row* GRMHD simulation. The left column shows the truth image, the middle columns an example reconstruction, and right the optimal VIDA filter applied to the reconstruction.

In this paper we focus on the forward modeling approaches from e.g. [Honma et al. \(2014\)](#); [Bouman et al. \(2016\)](#); [Akiyama et al. \(2017a,b\)](#); [Ikeda et al. \(2016\)](#); [Kuramochi et al. \(2018\)](#) and more specifically the `eht-imaging` package ([Chael et al. 2016, 2018](#)). The goal of the forward modeling approach is to find the im-

age, I , that minimizes the objective function

$$J(I) = \sum_{\text{data}} \alpha_d \chi_d^2(I) - \sum_{\text{regularizers}} \beta_r S_r(I). \quad (9)$$

Following [Paper IV](#), each χ^2 is defined solely from the data products from the EHT telescope, e.g., complex visibilities. The second term encapsulates our additional

assumptions, or regularizers, that are placed on the image. The $\alpha_d \beta_r$, are the “hyperparameters” that control the relative weighting of the regularizers and data products. For the list of the regularizers used, see [Paper IV](#). In an attempt to model the uncertainty in the image reconstructions, we used the same set of imaging hyperparameters as in [Paper IV](#). The resulting set of image reconstructions is called the “topset” and results in 1572 reconstructions per dataset.

3.2. Paper IV Tests

To validate VIDA, we applied it to a subset of the test set from [Event Horizon Telescope Collaboration et al. \(2019d\)](#). The sources we considered are shown in [Figure 2](#), and consist of two geometric crescents and a GRMHD simulation. The geometric crescent model is described by:

$$I(r, \theta) = I_0(1 - s \cos(\theta - \xi)) \frac{\delta(r - r_0)}{2\pi r_0}, \quad (10)$$

The infinitely thin ring is then convolved with a circular Gaussian with FWHM $10 \mu\text{as}$. Two orientations $\xi = 180^\circ$ and $\xi = 150^\circ$ are considered in this paper, and are shown in the left and middle panels of [Figure 2](#). For both orientations we took $r_0 = 22 \mu\text{as}$, $s = 0.46$, and $I_0 = 0.6 \text{ Jy}$. After blurring the ring, it is important to note that the effective radius (the intensity peak) is smaller than the original radius of the ring (see [Paper IV](#)). The amount the diameter is biased inwards is given approximately by:

$$d_{\text{blur}} = d_{\text{true}} - \frac{1}{8 \ln 2} \frac{\alpha^2}{d_{\text{true}}}, \quad (11)$$

where d_{true} is the diameter of the non-convolved ring ($44 \mu\text{as}$), and α is the FWHM of the Gaussian kernel ($\alpha = 10 \mu\text{as}$). Inverting this formula gives $d_{\text{blur}} \approx 43 \mu\text{as}$. If we also consider the finite resolution of the EHT array ($\sim 20 \mu\text{as}$) this is further decreased to $\approx 42 \mu\text{as}$. Therefore, we expect both VIDA and ReX to recover a diameter of $42 \mu\text{as}$.

3.3. ReX review

In [Event Horizon Telescope Collaboration et al. \(2019d\)](#), the method ReX was used to find the ring parameters of the image reconstructions. ReX assumes that a single ring-like feature dominates the image reconstruction, and then finds the ring by finding the image location that leads to a ring with minimal radial dispersion. ReX characterizes (see [Appendix A](#) and [Paper IV](#) for definitions) the ring through a diameter d , width w , brightness moments s and orientation ξ_s and a fractional dispersion of the diameter f_d . The diameter and

width and brightness profile of the ReX measurement are similar to VIDA’s measurement with the GGR filter. However, the fractional dispersion is not directly measured. Instead, VIDA measures the elliptical asymmetry of the ring. In [Appendix A](#) we demonstrate how f_d and τ are related if the dominant source of radial dispersion in the ring is due to ellipticity. Unlike VIDA, ReX requires that the dominant feature in an image is a ring. This restriction implies that ReX cannot be applied to images of non-ring structures such as those in [Figure 4](#).

3.4. Results

VIDA was run on each topset using the GGR filter with a constant flux background whose level was also a free parameter, giving 9 parameters in total. Some example reconstructions and corresponding optimal filters are shown in [Figure 2](#). The results are shown in [Figure 3](#). For the crescent models, we were able to recover the expected diameter d , width w , and azimuthal orientation ξ_s (black dotted lines in [Figure 3](#). The agreement between ReX and VIDA is excellent. The peak and overall width of the distribution for each parameter in [Figure 3](#) are consistent between ReX and VIDA. The ground truth values (black vertical lines) for the diameter, width, and brightness orientation ξ_s are also consistent with the ReX and VIDA results. While the slash strength is biased to be lower than the naive truth $s = 0.46$, this occurs in both VIDA and ReX. In fact, this bias is due to the blurring of the initial thin Gaussian ring. Convolution with the Gaussian kernel does not preserve the dipole moment of the angular distribution and instead lowers it. If we fit the thick blurred Gaussian ring with VIDA, we recover a slash strength of 0.32, consistent with the recovered slash strength in [Figure 3](#).

To compare VIDA and ReX’s measurement of asymmetry, we first note that an additional processing step is needed since the two definitions differ. ReX doesn’t directly measure τ but instead measures the fractional diameter dispersion of the ring f_d (see [Equation A5](#) for a definition). If we assume that the ring’s ellipticity dominates f_d , then f_d and τ are related by an invertible map. For more information about this conversion, see [Appendix A](#). In [Figure 3](#) we show ReX’s results after converting from f_d to τ . Comparing the two measurements of τ , we see that ReX’s measurement is consistently greater than VIDA’s. This bias is not unexpected given that when τ is small, the conversion described in [Appendix A](#) no longer applies. Instead, the fractional dispersion is dominated by random fluctuations in the ring diameter, creating a floor in f_d . If we then naively apply the previous conversion, as was done in [Figure 3](#), we will overestimate τ (see [Figure 8](#)).

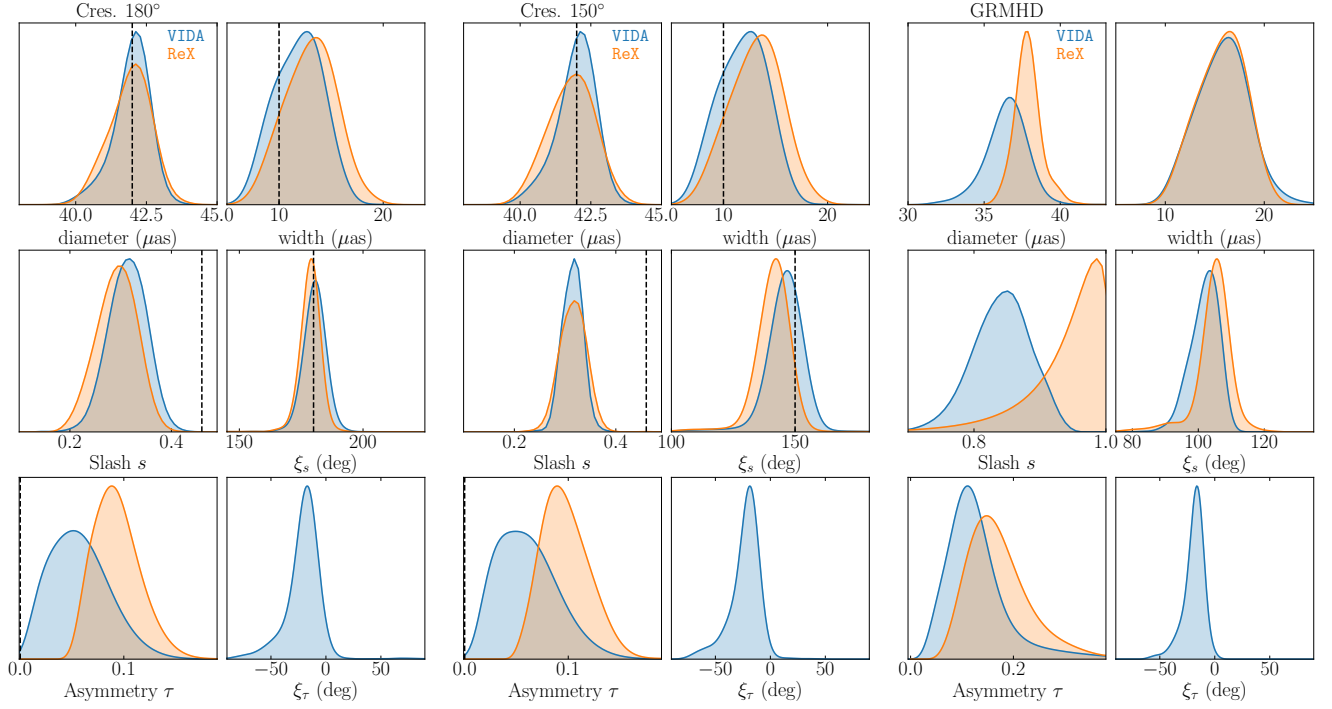


Figure 3. Results from VIDA (blue) and ReX (orange) being applied to the Paper IV reconstructions from April 11. Figure 2. The left-two and middle-two columns show the geometric crescent models’ results and the right-two for the GRMHD. In all instances, we found excellent agreement between VIDA (blue) and ReX (orange) for the ring diameter, width, asymmetry, and location of the azimuthal brightness. Furthermore, the crescent distributions for the diameter (after accounting for Equation 11), width, slash position angle ξ_s are consistent with the truth image (black dashed line). For the slash strength, s , and asymmetry, τ , both ReX, and VIDA give similar results but are biased from the truth. The origin of this bias is due to the finite resolution of the EHT array. Namely, when we fit the ground truth image with VIDA, we recover $s = 0.316$, which is consistent with the results from the image reconstructions.

The asymmetry orientation, ξ_τ , is only recovered by VIDA, so there is no ReX comparison. Similar results were found using the coverage from April 5, 6, and 10.

VIDA also recovers the orientation of the ring asymmetry ξ_τ . Interestingly, in all instances, we measure a similar distribution for ξ_τ irrespective of the intrinsic image. Furthermore, as is seen in Figure 2 the reconstructions themselves tend to have their semi-major axis in the north-south direction, suggesting this isn’t an artifact of VIDA. The origin of said bias will be explored in future work.

4. APPLYING VIDA TO ADDITIONAL TEST IMAGES

In the previous section, we saw that VIDA and ReX gave remarkably similar answers to problems that demonstrated similar ring-like structures. While ReX is limited to ring extraction, VIDA can be applied to any image, given a suitable filter function. This section will explore VIDA’s capabilities of extracting features from a broader range of potential sources. To accomplish this, we will consider the other non-ring test images from Paper IV: the symmetric disk and double Gaussian (see Figure 4).

4.1. Double Gaussian

Here we consider a source composed of a compact double with two circular Gaussian components. Each Gaussian has an FWHM of $20 \mu\text{as}$. One of the Gaussians is placed at the origin and has a flux of 0.27Jy , which we will call the NW component. The other Gaussian is at $\Delta\text{RA} = 30 \mu\text{as}$ and $\Delta\text{DEC} = -12 \mu\text{as}$ and has a flux of 0.33Jy and will be called the SE component. This type of source could arise when looking at AGN using VLBI images, such as the recent 3c 279 results (Kim et al. 2020).

To extract the reconstruction’s compact components, we used a filter with three asymmetric Gaussian components and constant background. Two of the Gaussian components were allowed to be arbitrary, while the third Gaussian component was forced to be large ($r_0 > 15 \mu\text{as}$). The reason for the third Gaussian was there tended to be a region of additional flux around the two dominant Gaussian components in the image reconstructions. This diffuse flux can be seen in the

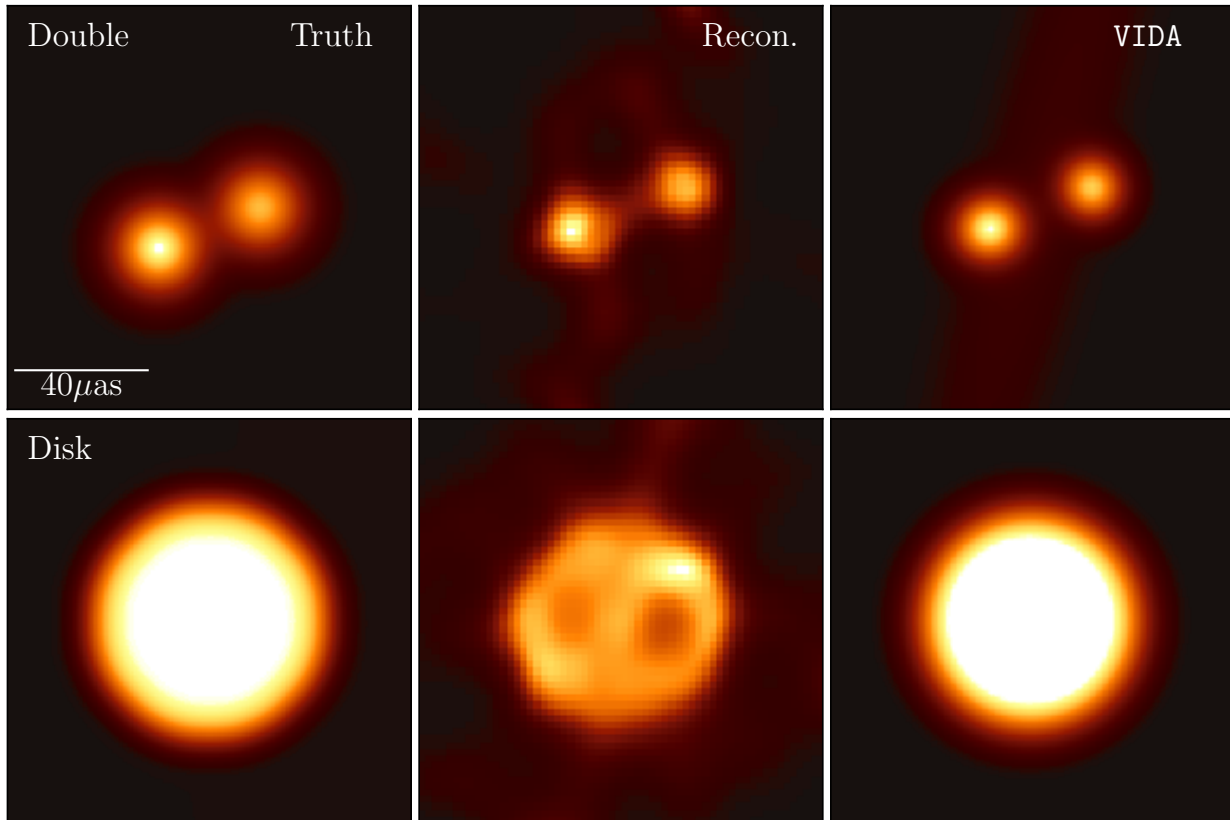


Figure 4. Results from applying VIDA to the non-ring test images from Paper IV where the left column shows the ground truth image, the middle an example reconstruction from the topset, and right the optimal filter from applying VIDA to the reconstruction. *Top:* Shows the results for the double image. *Bottom:* Shows the results for the disk. Overall VIDA can recover the intrinsic structure of both images.

top middle panel of Figure 4. If we didn’t include this third component, we found that the Gaussian components tended to be quite large to soak up the extra flux.

VIDA’s results for the double Gaussian are shown in Figure 5. Overall the size of each Gaussian, their separation, and flux ratio are reliably recovered. The asymmetry, τ , is larger than zero, but this is to be expected since the algorithm can only add asymmetry to the Gaussian components.

On April 6, we see that the asymmetry appears to be bimodal, and the parameter uncertainties are greater than the other days. This uncertainty was unexpected, given the relatively good EHT coverage on April 6. The origin of the discrepancy is a subset (10–15%) of image reconstructions on that day that exhibit an additional bright Gaussian feature. If we remove these reconstructions, we find that the results on April 6 are consistent with the other days.

4.2. Disk Image

The intrinsic image is a symmetric flat disk with a diameter of $70 \mu\text{as}$, which is then convolved with a Gaus-

sian with an FWHM of $10 \mu\text{as}$. The true image, an example reconstruction, and optimal filter for that reconstruction are shown in the lower left, middle panel, and right panel of Figure 4.

To encode the diameter of the disk we use FWHM of the disk filter:

$$d_{\text{filt}} = 2r_0 + 2\sqrt{2\log 2}\alpha, \quad (12)$$

where r_0 and α are described in Equation 1. We fit the disk filter to the ground truth image to calibrate the diameter definition to the disk’s true diameter. We found that the optimal filter for the true image had a $d_{\text{filt}} \approx 69 \mu\text{as}$. If we convolved the image by an additional $20 \mu\text{as}$ to take into account the finite resolution of the EHT array, we found $d_{\text{filt}} \approx 68 \mu\text{as}$. This is the value we use as the ground truth diameter in all comparisons below.

Figure 6 displays the results for VIDA applied to each day. Ignoring April 10, which has poor coverage compared to the other days, we find that the results are very consistent between days. On April 5, we find the

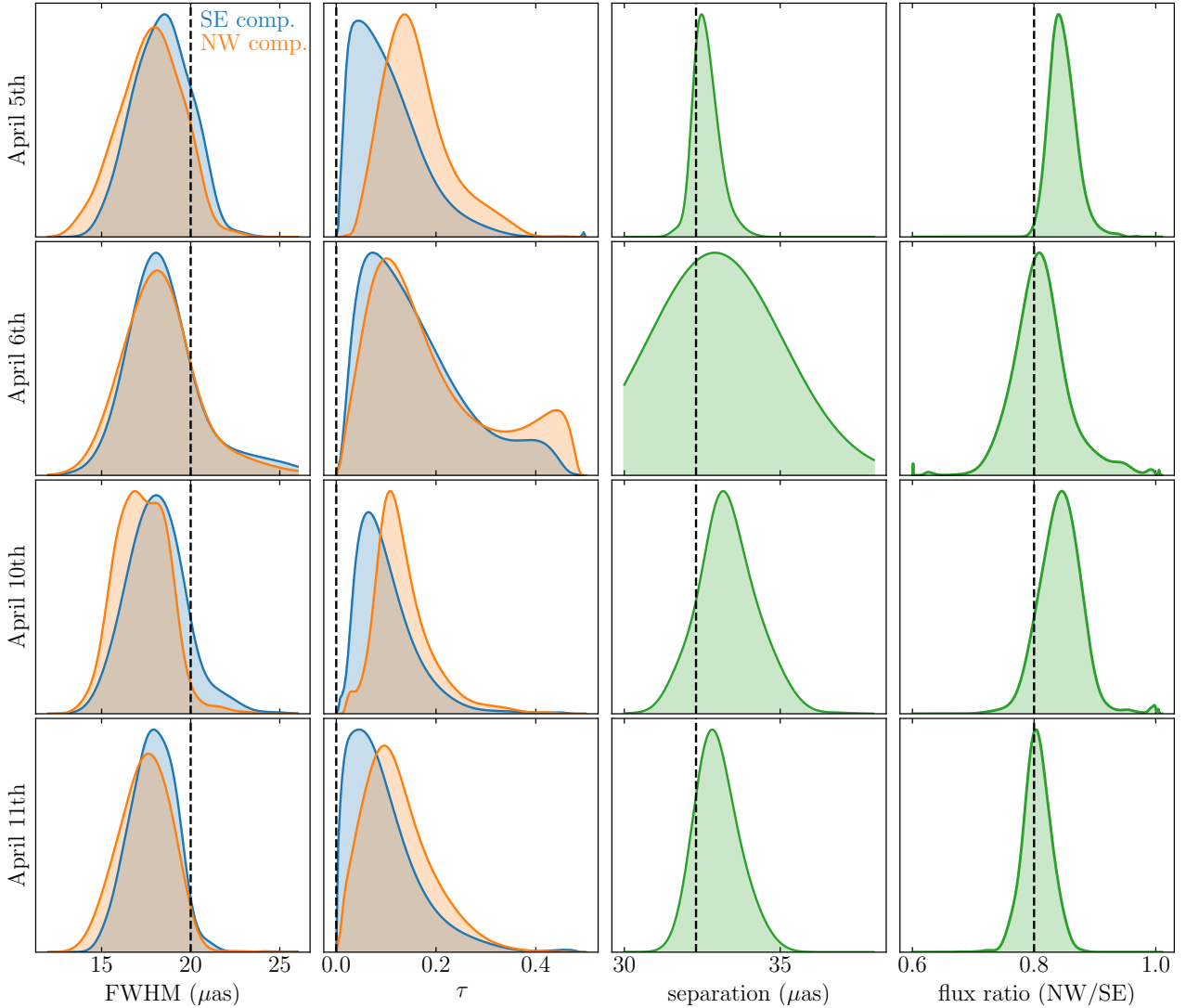


Figure 5. VIDA results for the two compact Gaussian components (blue for SE component and orange for the NW) in the double Gaussian test image. The green curves are for parameters that are a combination of the SE and NW components. On all days the true values are included in the parameter distributions found by VIDA. Note, that the broad distribution found on April 6th is due to an imaging artifact as discussed in the paper.

median diameter $d_{\text{filt}} = 65.7^{+0.42}_{-0.76} \mu\text{as}$ where the range are the 68% interval about the median. Similarly, on April 6th we find $d_{\text{filt}} = 65.6^{+0.40}_{-0.47} \mu\text{as}$, and April 11th $d_{\text{filt}} = 65.5^{+0.45}_{-0.80} \mu\text{as}$. This demonstrates that VIDA is robust to the slight difference in image reconstructions from different baseline coverages.

On April 10, however, we had a different result finding a bimodal diameter. Analyzing the reason for this, we found that images with $d_{\text{disk}} \approx 60 \mu\text{as}$ had a markedly different structure than the rest of the images. Given the distinct non-disk structure of the image, it is no surprise that VIDA struggles at recovering the correct diameter.

Comparing our result for the diameter to the true value, $68 \mu\text{as}$, we find that our result has a consistent bias of $\approx 2.4 \mu\text{as}$ on April 5, 6, and 11. Again, this appears to be an artifact of the imaging process. In Figure 7, the radial profiles of the truth (dotted lines), averaged image reconstructions⁴, and optimal filters are compared. VIDA does an excellent job of recovering the size of the images, which are similarly biased toward smaller radii. This suggests that the diameter bias is intrinsic to the topset used for this disk. As discussed above, it is un-

⁴ When averaging we first centered the images by computing the image centroid and normalized the images to have unit flux.

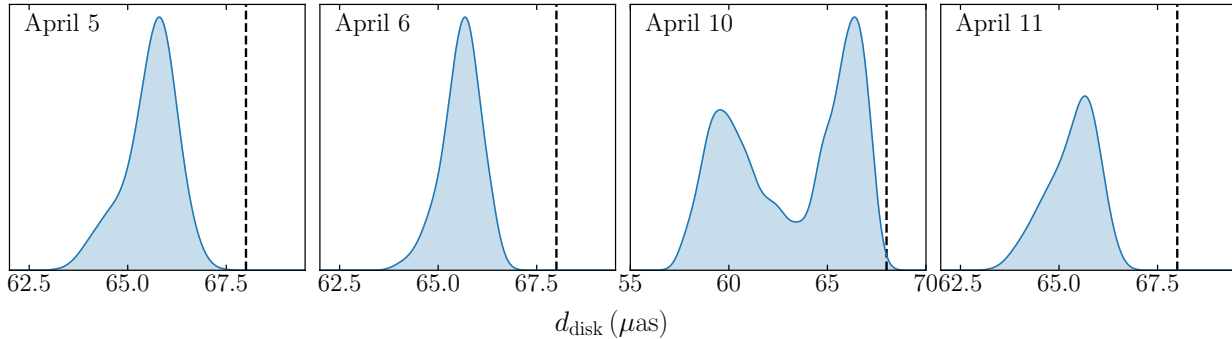


Figure 6. VIDA results of the diameter for the disk topset. The diameter is given by (12). Ignoring April 10, we consistently find that the diameter is $4\mu\text{as}$ smaller than the original image. The origin of this discrepancy is discussed in Figure 7. On April 10, which has poor coverage compared to the other days, the imaging gives two modes. One mode is similar to the other days, while the second fails to show a coherent disk structure giving the second peak in diameter at $60\mu\text{as}$.

likely that this is due to the finite resolution of the EHT array and is intrinsic to the imaging algorithms used.

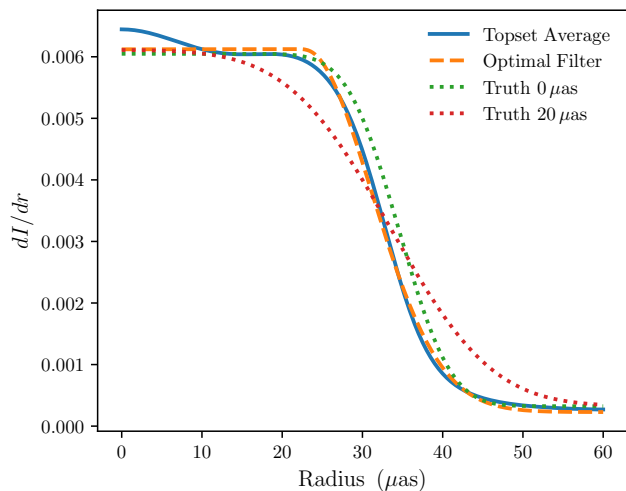


Figure 7. Results when applying VIDA to the average reconstruction from the topset on April 11. The images were normalized to unit flux and centered before averaging. The average radial profile is shown in solid blue. Comparing this to the optimal filter (orange dashed line) and the true profile (dotted lines), we see that the optimal filter matches the reconstruction’s radial profile but underestimates the ground truth image.

5. SUMMARY AND CONCLUSIONS

We present VIDA, a new image feature extraction technique appropriate for use by the EHT. VIDA adopts a forward modeling approach to extract quantitative image properties by approximating the image with a parameterized family of functions that encode the desired image properties.

A key feature of VIDA is its flexibility. Multiple image components have already been implemented, from which composite models of signification complexity can

be constructed. These include ring-like filters of particular relevance to EHT images, Gaussians, and constants.

The ability of VIDA has been demonstrated for several sources, each with over a thousand reconstructions. These include image reconstructions from simulated data produced from double Gaussians, slashed rings, and GRMHD simulations. In all cases, key quantitative features were accurately recovered where they appeared in the underlying image reconstructions. These include separations, orientations, ring diameters, widths, brightness profiles, and multiple measures of asymmetry. Application of these to the EHT observations of M 87 will be explored in future work.

The applicability of VIDA extends beyond EHT observations of M 87. The ability to create composite models with multiple components is naturally relevant to VLBI reconstruction of AGN, such as 3C 279, that is composed of multiple compact features (e.g., Kim et al. 2020).

It should be noted that image feature extraction methods, like VIDA, are generally most useful when strong priors may be placed on the image structure itself. That is, VIDA is primarily a method for quantifying what is already qualitatively apparent. Poorly chosen models can lead to significant parameters biases, as seen in Section 4.1, where an extra Gaussian blob was required to achieve acceptable results. However, because VIDA is an image characterization tool, not an imaging tool in and of itself, this presents only a very modest limitation on its utility.

Software: BlackBoxOptim.jl, eht-imaging, GR (Heinen et al. 1985–2019), Julia (Bezanson et al. 2017), matplotlib 3.3 (Hunter 2007), Pandas (McKinney et al. 2010), Python 3.8.3 (Van Rossum & Drake 2009), Scipy (Virtanen et al. 2020), ThemisPy, VIDA.jl

ACKNOWLEDGMENTS

This work was supported in part by Perimeter Institute for Theoretical Physics. Research at Perimeter Institute is supported by the Government of Canada through the Department of Innovation, Science and Economic Development Canada and by the Province of Ontario through the Ministry of Economic Development, Job Creation and Trade. PT receives support from the Natural Science and Engineering Research Council through the Alexander Graham Bell CGS-D scholarship. A.E.B. thanks the Delaney Family for their generous financial support via the Delaney Family John A. Wheeler Chair at Perimeter Institute. A.E.B. receives additional financial support from the Natural Sciences and Engineering Research Council of Canada through a Discovery Grant. We thank the National Science Foundation (AST-1716536, AST-1440254, AST-1935980) and the Gordon and Betty Moore Foundation (GBMF-5278) for financial support of this work. This work was supported in part by the Black Hole Initiative, which is funded by grants from the John Templeton Foundation and the Gordon and Betty Moore Foundation to Harvard University.

REFERENCES

- Akiyama, K., Kuramochi, K., Ikeda, S., et al. 2017a, *ApJ*, 838, 1, doi: [10.3847/1538-4357/aa6305](https://doi.org/10.3847/1538-4357/aa6305)
- Akiyama, K., Ikeda, S., Pleau, M., et al. 2017b, *AJ*, 153, 159, doi: [10.3847/1538-3881/aa6302](https://doi.org/10.3847/1538-3881/aa6302)
- Bezanson, J., Edelman, A., Karpinski, S., & Shah, V. B. 2017, *SIAM review*, 59, 65.
<https://doi.org/10.1137/141000671>
- Bhattacharyya, A. 1943, *Bull. Calcutta math. Soc.*, 35, 99.
<https://ci.nii.ac.jp/naid/10030997340/en/>
- Bouman, K. L., Johnson, M. D., Zoran, D., et al. 2016, in *Proceedings of the IEEE Conference on Computer Vision and Pattern Recognition (CVPR)*
- Broderick, A. E., Pesce, D. W., Tiede, P., Pu, H.-Y., & Gold, R. 2020, *The Astrophysical Journal*, 898, 9, doi: [10.3847/1538-4357/ab9c1f](https://doi.org/10.3847/1538-4357/ab9c1f)
- Chael, A. A. 2019, PhD thesis, Harvard University, Graduate School of Arts & Sciences
- Chael, A. A., Johnson, M. D., Bouman, K. L., et al. 2018, *ApJ*, 857, 23, doi: [10.3847/1538-4357/aab6a8](https://doi.org/10.3847/1538-4357/aab6a8)
- Chael, A. A., Johnson, M. D., Narayan, R., et al. 2016, *ApJ*, 829, 11, doi: [10.3847/0004-637X/829/1/11](https://doi.org/10.3847/0004-637X/829/1/11)
- Clark, B. G. 1980, *A&A*, 89, 377
- Das, S., & Suganthan, P. N. 2011, *IEEE Transactions on Evolutionary Computation*, 15, 4, doi: [10.1109/TEVC.2010.2059031](https://doi.org/10.1109/TEVC.2010.2059031)
- Duda, R. O., & Hart, P. E. 1972, *Commun. ACM*, 15, 11–15, doi: [10.1145/361237.361242](https://doi.org/10.1145/361237.361242)
- Event Horizon Telescope Collaboration, Akiyama, K., Alberdi, A., et al. 2019a, *ApJL*, 875, L3, doi: [10.3847/2041-8213/ab0c57](https://doi.org/10.3847/2041-8213/ab0c57)
- . 2019b, *ApJL*, 875, L1, doi: [10.3847/2041-8213/ab0ec7](https://doi.org/10.3847/2041-8213/ab0ec7)
- . 2019c, *ApJL*, 875, L6, doi: [10.3847/2041-8213/ab1141](https://doi.org/10.3847/2041-8213/ab1141)
- . 2019d, *ApJL*, 875, L4, doi: [10.3847/2041-8213/ab0e85](https://doi.org/10.3847/2041-8213/ab0e85)
- . 2019e, *ApJL*, 875, L5, doi: [10.3847/2041-8213/ab0f43](https://doi.org/10.3847/2041-8213/ab0f43)
- Frieden, B. R. 1972, *Journal of the Optical Society of America* (1917-1983), 62, 511.
<http://adsabs.harvard.edu/abs/1972JOSA...62..511F>
- Goffe, W. L. 01 Oct. 1996, *Studies in Nonlinear Dynamics & Econometrics*, 1, doi: <https://doi.org/10.2202/1558-3708.1020>
- Gull, S. F., & Daniell, G. J. 1978, *Nature*, 272, 686, doi: [10.1038/272686a0](https://doi.org/10.1038/272686a0)
- Heinen, J., et al. 1985–2019, *GR Framework*.
<https://gr-framework.org/>
- Honma, M., Akiyama, K., Uemura, M., & Ikeda, S. 2014, *PASJ*, 66, 95, doi: [10.1093/pasj/psu070](https://doi.org/10.1093/pasj/psu070)

- Hough, P. V. C. 1964, *Optical Engineering*, 2, 379, doi: [10.1117/12.7971269](https://doi.org/10.1117/12.7971269)
- Hunter, J. D. 2007, *Computing in Science & Engineering*, 9, 90, doi: [10.1109/MCSE.2007.55](https://doi.org/10.1109/MCSE.2007.55)
- Högbom, J. A. 1974, *Astronomy and Astrophysics Supplement Series*, 15, 417.
<http://adsabs.harvard.edu/abs/1974A%26AS...15..417H>
- Ikeda, S., Tazaki, F., Akiyama, K., Hada, K., & Honma, M. 2016, *PASJ*, 68, 45, doi: [10.1093/pasj/psw042](https://doi.org/10.1093/pasj/psw042)
- Kim, J., Krichbaum, T. P., Broderick, A. E., et al. 2020, *A&A*, doi: [10.1051/0004-6361/202037493](https://doi.org/10.1051/0004-6361/202037493)
- Kullback, S., & Leibler, R. A. 1951, *Ann. Math. Statist.*, 22, 79, doi: [10.1214/aoms/1177729694](https://doi.org/10.1214/aoms/1177729694)
- Kuramochi, K., Akiyama, K., Ikeda, S., et al. 2018, *The Astrophysical Journal*, 858, 56, doi: [10.3847/1538-4357/aab6b5](https://doi.org/10.3847/1538-4357/aab6b5)
- McKinney, W., et al. 2010, in *Proceedings of the 9th Python in Science Conference*, Vol. 445, Austin, TX, 51–56
- Mogensen, P. K., & Riseth, A. N. 2018, *Journal of Open Source Software*, 3, 615, doi: [10.21105/joss.00615](https://doi.org/10.21105/joss.00615)
- Narayan, R., & Nityananda, R. 1986, *Annual Review of Astronomy and Astrophysics*, 24, 127, doi: [10.1146/annurev.aa.24.090186.001015](https://doi.org/10.1146/annurev.aa.24.090186.001015)
- Ranganath, R., Tran, D., Alotaibi, J., & Blei, D. 2016, in *Advances in Neural Information Processing Systems 29*, ed. D. D. Lee, M. Sugiyama, U. V. Luxburg, I. Guyon, & R. Garnett (Curran Associates, Inc.), 496–504.
<http://papers.nips.cc/paper/6091-operator-variational-inference.pdf>
- Schwab, F. R. 1984, *AJ*, 89, 1076, doi: [10.1086/113605](https://doi.org/10.1086/113605)
- Schwarz, U. J. 1978, *Astronomy and Astrophysics*, 65, 345.
<http://adsabs.harvard.edu/abs/1978A%26A....65..345S>
- Van Rossum, G., & Drake, F. L. 2009, *Python 3 Reference Manual* (Scotts Valley, CA: CreateSpace)
- Virtanen, P., Gommers, R., Oliphant, T. E., et al. 2020, *Nature Methods*, 17, 261, doi: <https://doi.org/10.1038/s41592-019-0686-2>

APPENDIX

A. ReX RING PARAMETER DEFINITIONS

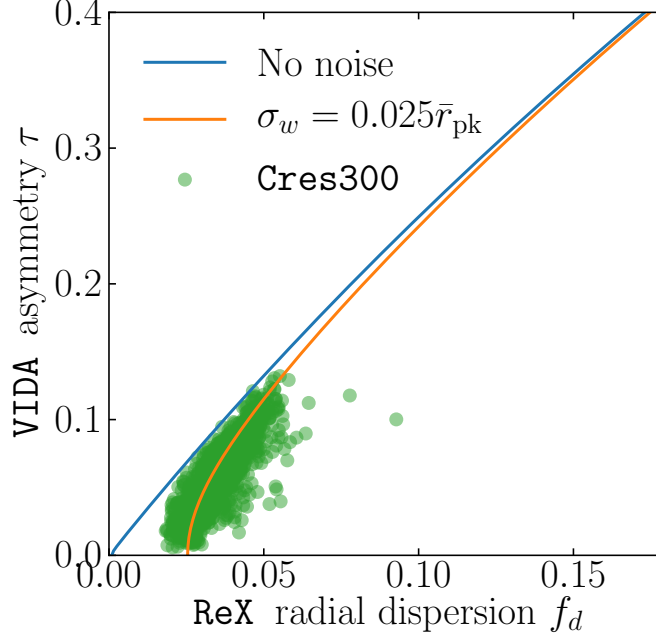


Figure 8. Comparison of the ReX’s fractional radial dispersion and VIDA’s τ asymmetry parameter. The blue curve shows the conversion for the case of an ellipse, the orange curve is an ellipse with a constant white noise fluctuation in the found radius, with a variance of $0.025^2 \bar{r}_{\text{pk}}^2$, and the green points are the results of fitting the Cres150 topset in Section 3 with both ReX and VIDA.

The first step in ReX (see Paper IV, for details) is to identify the dominant ring in the image. Given a center position (x, y) , ReX samples the image in radius r and azimuthal angle θ obtaining a intensity map $I(r, \theta|x, y)$. Then for that central map, the radius of the ring is taken as the azimuthally averaged peak brightness:

$$\begin{aligned} r_{\text{pk}}(\theta|x, y) &= \text{argmax}[I(r, \theta|x, y)]_r \\ \bar{r}_{\text{pk}} &= \langle r_{\text{pk}}(\theta|x, y) \rangle_{\theta \in [0, 2\pi]}. \end{aligned} \quad (\text{A1})$$

This provides a different “radius” for every point (x, y) in the image. To find the dominant ring in the image the fractional radius spread is minimized:

$$(x_0, y_0) = \text{argmin} \left[\frac{\sigma_{\bar{r}}(x, y)}{\bar{r}_{\text{pk}}(x, y)} \right], \quad (\text{A2})$$

where $\sigma_{\bar{r}}(x, y) = \langle (r_{\text{pk}}(\theta|x, y) - \bar{r}_{\text{pk}})^2 \rangle$, is the radial dispersion. The diameter in the image is then given by:

$$d = 2\bar{r}_{\text{pk}}(x_0, y_0). \quad (\text{A3})$$

To relate this to VIDA’s definition we consider an ellipse with semi-major axis a and semi-minor axis b . Then VIDA parameterizes this ellipse with $d_0 = 2r_0 = 2\sqrt{ab}$ and $\tau = 1 - b/a$. The relationship between r_0 and r_{pk} is then given by

$$\bar{r}_{\text{pk}} = \frac{r_0}{\sqrt{1-\tau}} \frac{1}{2\pi} \int_0^{2\pi} \sqrt{1 - \epsilon^2(\tau) \sin^2(\theta)} d\theta = \frac{2}{\pi} \frac{r_0}{\sqrt{1-\tau}} E(\epsilon(\tau)), \quad (\text{A4})$$

where $E(x)$ is the complete Elliptic integral of the second kind and $\epsilon(\tau) = \sqrt{1 - (1-\tau)^2}$ is the orbital eccentricity.

ReX's measure of circularity of the ring is provided by the radial fractional dispersion:

$$f_d = \frac{\sigma_{\bar{r}}}{\bar{r}_{\text{pk}}}. \quad (\text{A5})$$

To compare **ReX**'s asymmetry measure, f_d , to **VIDA**'s, we need to relate f_d to $\tau = 1 - b/a$

$$f_d(\tau) = \frac{\sqrt{1 - \epsilon(\tau)^2 - 4/\pi^2 E^2(\epsilon)}}{\sqrt{1 - \tau}} = \frac{\sqrt{(1 - \tau)^2 - 4/\pi^2 E^2(\epsilon)}}{\sqrt{1 - \tau}} \quad (\text{A6})$$

[Equation A5](#) is then used to convert this to a fractional diameter spread. Using linear interpolation we invert the function achieving a map from f_d to τ . One important thing to note is that this conversion assumes that the image is a perfect ellipse. In general, this will not be true for the image reconstructions and expect that the **ReX** asymmetry may be different than the **VIDA** measurement. To model this we consider r_{pk} modified by a white noise ϵ_θ term with dispersion proportional to the average radius $\langle \epsilon_\theta \epsilon_{\theta'} \rangle = \sigma_w^2 \bar{r}_{\text{pk}}^2 \delta(\theta - \theta')$. In this base the average peak radius is unchanged since ϵ has mean 0. However, the additional noise does impact the radial dispersion:

$$\sigma_{\bar{r}} \rightarrow \sigma_{\bar{r}} + 2 \langle \epsilon_\theta r_{\text{pk}}(\theta) \rangle + \langle \epsilon_\theta^2 \rangle. \quad (\text{A7})$$

When we have a circular ring then this just becomes $\langle \epsilon_\theta^2 \rangle = \sigma_\epsilon^2 \bar{r}_{\text{pk}}^2$ adding a constant floor. [Figure 8](#) shows the conversion when the ring is elliptical and compares it to the results of the Cres150 topset of [Section 3](#).

The width of the ring is defined by finding the FWHM at a fixed θ ray, and then averaging over θ ,

$$w = \langle \text{FWHM}_r [I(r, \theta | x_0, y_0) - I_{\text{floor}}] \rangle_\theta. \quad (\text{A8})$$

The flux floor is given by $I_{\text{floor}} = \langle I(r = 50 \mu\text{as}, \theta) \rangle_\theta$ and is included to avoid biasing the measurement due to the low level flux present in the image. This is similar to including the constant flux filter during the **VIDA** extraction.

In order to characterize the azimuthal profile of the ring (ξ_s and s for **VIDA**) we consider the azimuthal moments of the ring. Namely, the orientation ξ_s is given by:

$$\xi_s = \left\langle \text{Arg} \left[\int_0^{2\pi} I(r, \theta | x_0, y_0) e^{i\theta} d\theta \right] \right\rangle_{r \in [r_{\text{in}}, r_{\text{out}}]}, \quad (\text{A9})$$

where $r_{\text{in}} = (d - w)/2$ and $r_{\text{out}} = (d + w)/2$. The strength of the slash is given by

$$s = 2 \left\langle \frac{\left| \int_0^{2\pi} I(r, \theta | x_0, y_0) e^{i\theta} d\theta \right|}{\int_0^{2\pi} I(r, \theta | x_0, y_0) d\theta} \right\rangle. \quad (\text{A10})$$

Note that the factor of 2 is included to match **VIDA**'s definition ([Equation 4](#)).